RSC Advances

PAPER

View Article Online
View Journal | View Issue

Cite this: *RSC Adv.*, 2025, **15**, 16654

Microwave-assisted synthesis of a zirconium-based MOF as an efficient catalyst for one-pot synthesis of xanthene derivatives: *in silico* study as a potential anti-HIV RNA†

Mohammed S. Alsalhi,[a] Mahmoud Tarek,*[b] Gehad E. Said, *[b] Abdulrahman A. Almehizia, [c] Ahmed M. Naglah *[c] and Tamer K. Khatab[d]

Firstly, construction and characterization of a novel Zr/VitB$_3$ metal organic framework have been described. The physicochemical analysis and morphological properties of Zr-MOF has been accomplished by IR, SEM, EDX, TEM, and XRD. Cyclic diketones and various aromatic aldehydes were efficiently and ecologically benignly condensed in a single pot, yielding a range of tetrahydroxanthenediones in good to excellent yields. The utilization of a heterogeneous catalyst, solventless conditions, and a straightforward process that is atom-economical and yields low *E*-factor values are some of the benefits of this multicomponent reaction. The catalyst can be used up to three times and is completely recyclable. Advantages include a clean methodology, high yield, and straightforward catalyst preparation. Additionally, the study investigates the potential binding interactions of Zr-MOF with the HIV-RNA major groove, revealing its exceptional stability and strong binding affinity. The binding energy score of the Zr-MOF with HIV-RNA was found to be remarkably low at −12.32 kcal mol^{-1}, indicating its potential to significantly outperform the reference molecule, nevirapine, which showed a higher *E*-score of −4.98 kcal mol^{-1}. Xanthene derivatives were also evaluated for their binding affinity to the viral major groove, with energy scores ranging from −5.55 to −6.40 kcal mol^{-1}, further indicating a promising potential for anti-HIV drug design. These findings underscore the potential of Zr-MOF and xanthene derivatives as potent candidates for HIV treatment, surpassing the reference molecule in terms of binding strength.

Received 27th April 2025
Accepted 12th May 2025

DOI: 10.1039/d5ra02959g

rsc.li/rsc-advances

1. Introduction

Heterocyclic compounds, including xanthene and its derivatives, possess substantial medical, biological, and pharmacological properties, involving anti-inflammatory, antibacterial, antiviral, antidepressant, and antimalarial properties.[1–3] Recently, they have attracted significant interest from researchers (Fig. 1). They have been utilized in dyes,[4] removal of mercury ions,[5] photodynamic treatment,[6,7] pH-sensitive fluorescent materials for the visualization of biomolecular assemblies,[8] and laser technologies.[9–11] Additionally, they are antagonists of the paralyzing effects of Zoloft amine.[12]

Recently, a variety of catalysts have been developed for the synthesis of xanthene derivatives, including succinic acid,[13] γ-Fe_2O_3 hydroxyapatite-Fe^{2+} nanoparticles,[14] iron oxide nanoparticles supported on SBA-15 (FeNP@SBA-15),[15] acetic acid (CH_3COOH),[16] silica sulfuric acid,[17] succinimide-*N*-sulfonic acid,[18] and sulfamic acid.[19,20] But all of the synthetic methods needed more solvent, toxic and costly catalysts, longer reaction times, and higher temperatures, and gave worse yields than the previously developed method. In order to overcome these limitations, we began to build metal–organic frameworks, which are alternative catalysts with several advantages.[21]

Because of their versatility, Metal–Organic Frameworks (MOFs) are materials that can be used in a variety of ways in the synthesis of organic molecules.[22–25] MOFs are crystalline solids composed of a porous network of metal ions or clusters joined by organic ligands.[26] They are useful in many organic synthesis applications because of their unique properties, which include chemical stability, wide surface area, and tunable pore size.[27] Because of their unique pore sizes and chemical environments, the metal sites in MOFs can act as catalysts or catalyst supports

[a]*Department of Pharmaceutical Chemistry, College of Pharmacy, King Saud University, P.O. Box 2457, Riyadh, 11451, Saudi Arabia*

[b]*Chemistry Department, Faculty of Science, Mansoura University, 35516 Mansoura, Egypt. E-mail: mahmoudtarek.tm@gmail.com; gehadsaid@mans.edu.eg*

[c]*Drug Exploration & Development Chair (DEDC), Department of Pharmaceutical Chemistry, College of Pharmacy, King Saud University, P.O. Box 2457, Riyadh 11451, Saudi Arabia. E-mail: anaglah@ksu.edu.sa*

[d]*Organometallic and Organometalloid Chemistry Department, National Research Centre, 33 ElBehouth St., Dokki, 12622 Giza, Egypt*

† Electronic supplementary information (ESI) available. See DOI: https://doi.org/10.1039/d5ra02959g

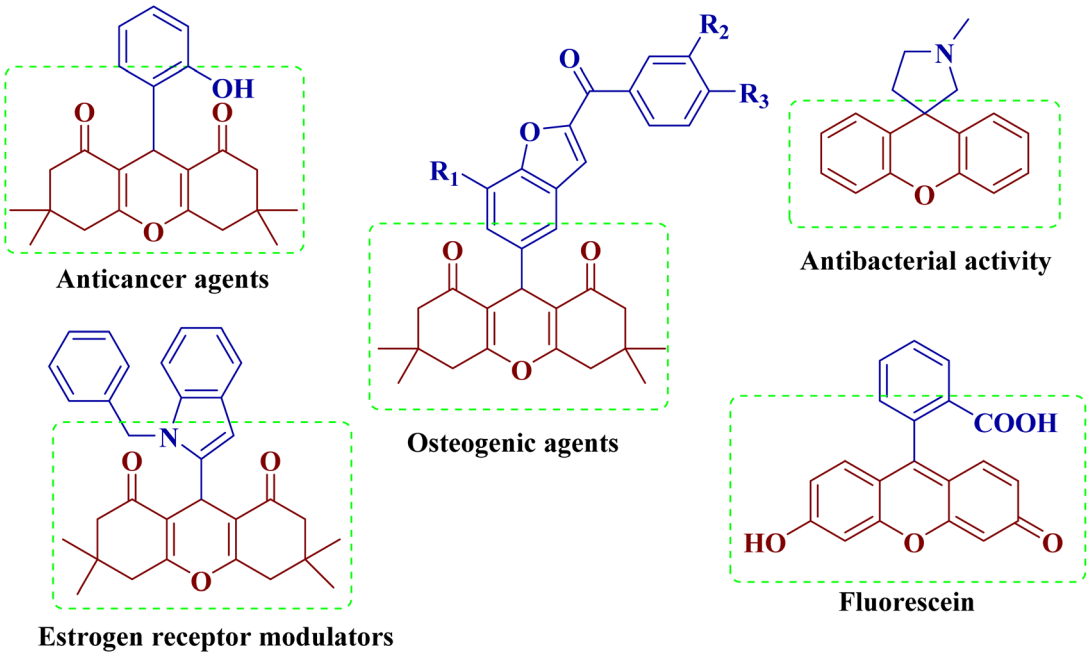

Fig. 1 Relevant bioactive xanthene-incorporated frameworks.

in organic reactions, facilitating oxidation, reduction, and polymerization, as well as selectively adsorbing specific molecules. This property can be used to separate and purify organic compounds.[28–31] Overall, MOFs high activity, selectivity, and recyclability make them exceptional heterogeneous catalysts for chemical synthesis. MOF catalysts offer enormous potential to address significant issues in modern organic chemistry with further research.

Over the past 25 years, since the discovery of HIV, significant health concerns have emerged. Initial estimates indicated that more than 33 million people worldwide were infected with HIV, resulting in more than 25 million deaths from virus-related complications. However, in the last decade these numbers have slowed. This is due to the development of several drugs that target key enzymes in the HIV viral cycle, such as proteases, reverse transcriptase, and integrases. These treatments have proven effective and have contributed to reducing mortality rates, especially in people with low viral loads. To date, developing a fully effective drug remains a significant challenge due to the ability of this type of virus to adapt and become drug-resistant.[32–35]

Molecular docking is one of the most prominent computer simulation techniques to emerge in recent decades, contributing to time, cost, and precision savings in the design and discovery of new drugs. Since the 1980s, this type of docking has become an essential part of drug discovery. With the advancement of computational technology, this field has witnessed significant progress, making results more accurate and realistic when measuring the strength of the binding between small molecules, known as ligands, and target receptors, such as proteins and DNA. This study is among the first to demonstrate the relationship between metal–organic frameworks and HIV RNA, using docking software, and represents the beginning of future research and experimental opportunities in this field.[22,36–46]

2. Practical and experimental

2.1. Materials and characterization

All materials, instrumentation details, and characterization data related to the chemical procedures and the catalyst are provided in the ESI.†

2.2. Microwave-assisted synthesis (MAS) of Zr-MOF

Microwave-assisted synthesis (MAS) is commonly utilized and considered an effective and innovative approach for generating MOF materials,[47,48] as it facilitates quick and uniform heating of the complete reactant mixture in a brief time frame. Two programmable microfluidic syringes were used to inject a zirconium solution (0.178 g, 1 mmol zirconium nitrate dissolved in 15 mL of deionized water and ethylene glycol) and vitamin B_3 (0.246 g, 1 mmol vitamin B_3 solubilized in the same volume of solvents) into a PTFE tubular reactor within a microwave oven at 180 °C for a duration of 10 hours. Following this, the mixture was subjected to centrifugation at 7000 rpm and washes with warm DIW and acetone, resulting in pale yellow crystals of Zr-Vit B_3/MOF.

2.3. Organic synthesis and structure elucidation

2.3.1. 1,8-Dioxo-octahydroxanthenes synthesis (Table 3, entries 1–12) catalyzed by Zr-Vit B_3/MOF. A catalytic amount of Zr-Vit B_3/MOF NPs (50 mg) for a suitable amount of time combined with an aromatic aldehyde, and two moles of dimedone then agitated and heated to 60–70 °C. After the final product was produced, the reaction mixture was allowed to cool to room temperature, and the catalyst was filtered away using

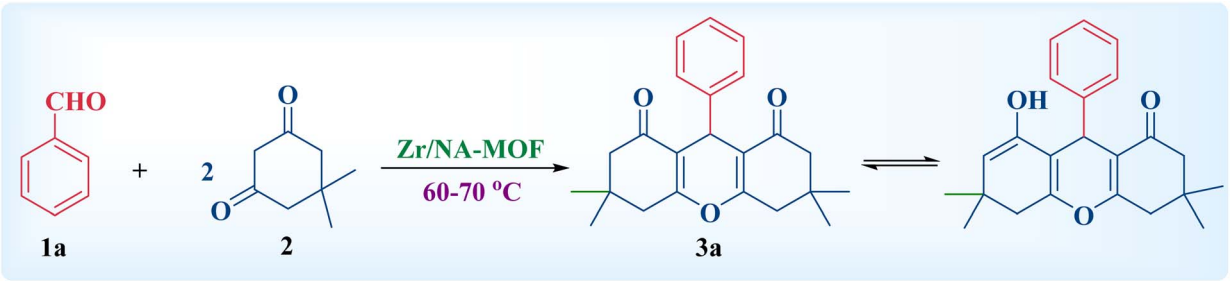

Scheme 1 Synthesis of 1,8-dioxo-octahydroxanthene derivative (**3a**) as a model example.

ethanol. In order to comprehend the catalytic mechanism generating high yields of octahydroxanthenediones, the reaction was investigated. The product structures, melting temperatures, yield percentages, and reaction times for compounds **3a–3l** are compiled in Table 3 and Scheme 1.

2.3.2. 9-(2-(4-Bromophenyl)-2-chlorovinyl)-3,3,6,6-tetramethyl-3,4,5,6,7,9-hexahydro-1*H*-xanthene-1,8(2*H*)-dione (3g).

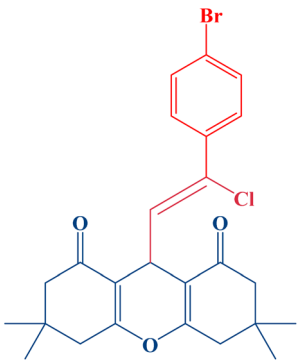

White solid powder; yield 90%; m.p. = 260–262 °C. ^{1}H NMR (400 MHz) ($CDCl_3$): δ (ppm) = 1.10 (s, 6H, $2CH_3$), 1.12 (s, 6H, $2CH_3$), 2.25 (s, 4H, $2CH_2$), 2.39 (s, 4H, $2CH_2$), 4.46 (d, J = 8.80 Hz, 1H, CH_{pyran}), 6.52 (d, J = 8.80 Hz, 1H, CH=C), 7.21–7.89 (m, 4H, Ar-H). ^{13}C NMR (100 MHz) (δ/ppm): 22.31, 22.59 (2C), 23.61 (2C), 25.09 (2C), 35.32 (2C), 44.95 (2C), 72.13 (2C), 110.09 (2C), 124.30, 128.24 (2C), 132.45 (2C), 133.38 (2C), 136.11, 161.48, 195.27. Anal. calcd for $C_{25}H_{26}BrClO_3$ (488.08): C, 61.30; H, 5.35%. Found: C, 61.39; H, 5.29%.

2.3.3. 3,3,6,6-Tetramethyl-9-(4-(trifluoromethyl)phenyl)-3,4,5,6,7,9-hexahydro-1*H*-xanthene-1,8(2*H*)-dione (3k).

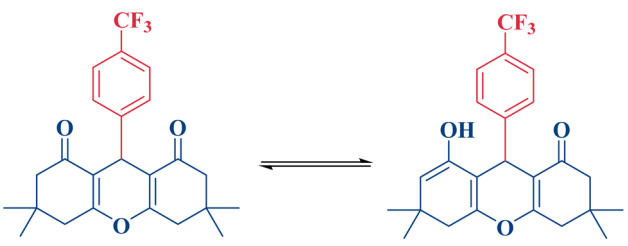

White powder; yield 90%; m.p. = 130–132 °C. ^{1}H NMR (500 MHz) ($CDCl_3$): δ (ppm) = 1.09 (s, 6H, $2CH_3$), 1.21 (s, 6H, $2CH_3$), 2.32–2.43 (m, 6H, $3CH_2$), 4.65 (s, 1H, CH_{pyran}), 5.47 (s, 1H, CH=C), 7.00 (d, 2H, J = 7.00 Hz, Ar-H), 7.21 (d, 2H, J = 6.50 Hz, Ar-H), 11.90 (s, 1H, OH). ^{13}C NMR (125 MHz) (δ/ppm): 27.37 (2C), 29.54 (2C), 31.37 (2C), 32.32, 46.43, 47.00 (2C), 115.28 (2C), 126.11, 128.16 (3C), 128.29 (3C), 131.5 (2C), 136.71, 189.42, 190.68. Anal. calcd for $C_{24}H_{25}F_3O_3$ (418.18): C, 68.89; H, 6.02%. Found: C, 68.80; H, 6.09%.

2.3.4. 3,3,6,6-Tetramethyl-9-[3-(4-chlorophenyl)-1-phenyl-1*H*-pyrazol-4-yl]3,4,5,6,2,9-hexahydro-8-hydroxyxanthene-1-one (3l).

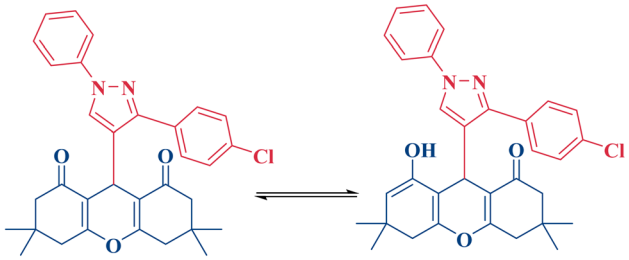

White powder; yield 92%; m.p. = 280–282 °C. ^{1}H NMR (400 MHz) ($CDCl_3$): δ (ppm) = 0.98 (s, 6H, $2CH_3$), 0.91 (s, 6H, $2CH_3$), 1.95 (d, 1H, CH), 1.99 (d, 1H, CH), 2.10 (s, 4H, $2CH_2$), 5.67 (s, 1H, CH), 7.29–7.67 (m, 11H, Ar-H, CH-pyrazol, 1H-enolic), 12.09 (s, 1H, OH). ^{13}C NMR (100 MHz) (δ/ppm): 25.66, 28.22, 31.67, 46.25, 46.89 [$3\underline{C}H_2$ + $4\underline{C}H_3$ + C of pyran + quaternary (2C)], 118.19, 118.19, 119.77, 121.91, 127.33, 128.14, 129.76, 130.49, 131.31, 132.09, (12Ar + 2pyrazole C + 3C olefinic), 139.93 (–C=N), 150.16 (O–C=C), 189.40, 189.37 (2CO). Anal. calcd for $C_{32}H_{31}ClN_2O_3$ (526.20): C, 72.92; H, 5.93; N, 5.32%. Found: C, 72.88; H, 5.96; N, 5.39%.

2.4. Docking software, enzyme and source

The X-ray crystal structure of the peroxisome proliferator-activated receptor (HIV-RNA and transpeptidase), obtained from PDB ID: 2L94 and 8TCM were opened using MOE2015.10 software. The protein–ligand docking process begins with preparing the target protein structure, typically retrieved from the Protein Data Bank (PDB). Using MOE, non-essential molecules such as water, ions, and duplicate chains are removed, missing hydrogen atoms are added, partial charges are assigned, and the structure is energy-minimized to resolve steric clashes. Active sites are then identified using MOE's Site Finder tool, which detects surface cavities based on geometric and chemical properties, with the binding site usually selected based on the presence of a co-crystallized ligand or known

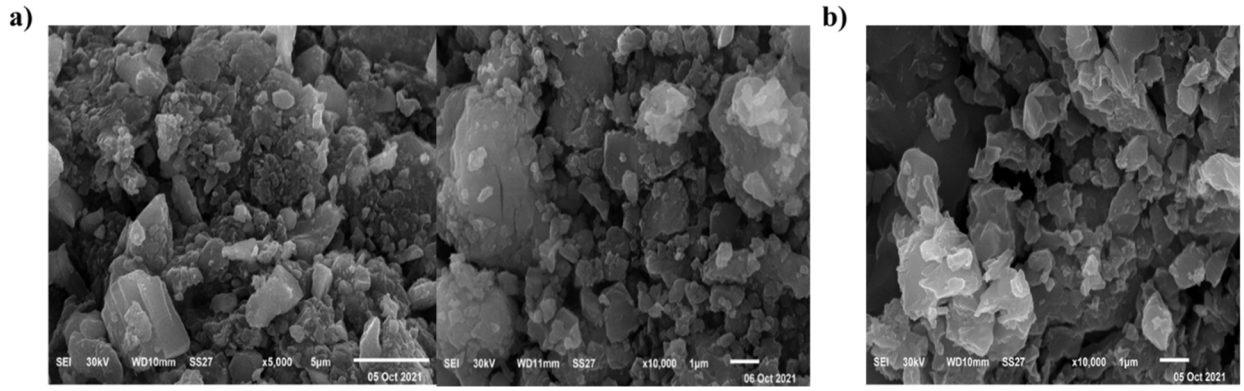

Fig. 2 (a) SEM images of Zr-Vit B_3/MOF nanostructures and (b) SEM image of Zr-Vit B_3/MOF after reuse.

catalytic residues. Ligands are either drawn in MOE or imported from databases like PubChem or tools like ChemDraw, followed by 3D protonation, energy minimization, and conformational analysis, including generation of tautomers or stereoisomers if needed. Docking is set up by selecting the prepared ligands and binding site, specifying parameters such as the placement method (*e.g.*, Triangle Matcher), scoring functions (*e.g.*, London dG for initial placement and GBVI/WSA dG for refinement), and the number of poses to retain. Finally, MOE performs the docking by generating multiple ligand poses, scoring them based on shape complementarity and interaction energies, and selecting the best conformations based on scoring, RMSD, and key molecular interactions.

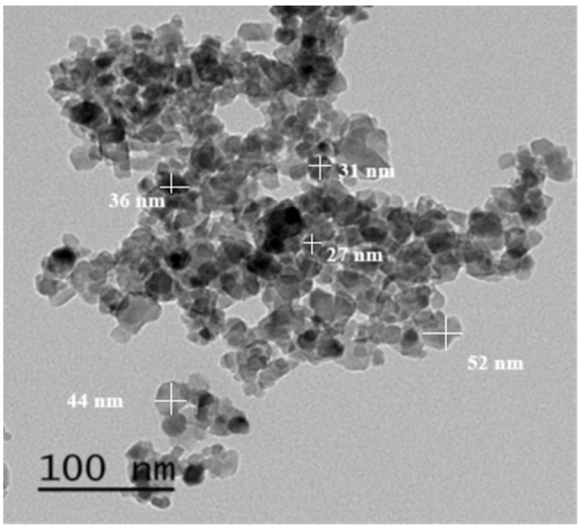

Fig. 4 TEM image of Zr-Vit B_3/MOF nanostructures.

3. Results and discussion

3.1. SEM analysis

SEM images of synthesized Zr-Vit B_3/MOF nanostructures were displayed in order to investigate their structural, chemical, and morphological features. Fig. 2a shows the sample surface of the spherical nanostructures Zr-Vit B_3/MOF and SEM images of synthesized Zr-MOF after reusability study (Fig. 2b), showed that there was no significant difference in the catalyst's surface morphology after it was separated and reused again. This is a source of strength for our catalyst, as it indicates its strong stability even after multiple uses.

3.2. EDX analysis

Energy-dispersive X-ray spectroscopy (EDX), commonly employed alongside SEM, is a crucial technique for analyzing

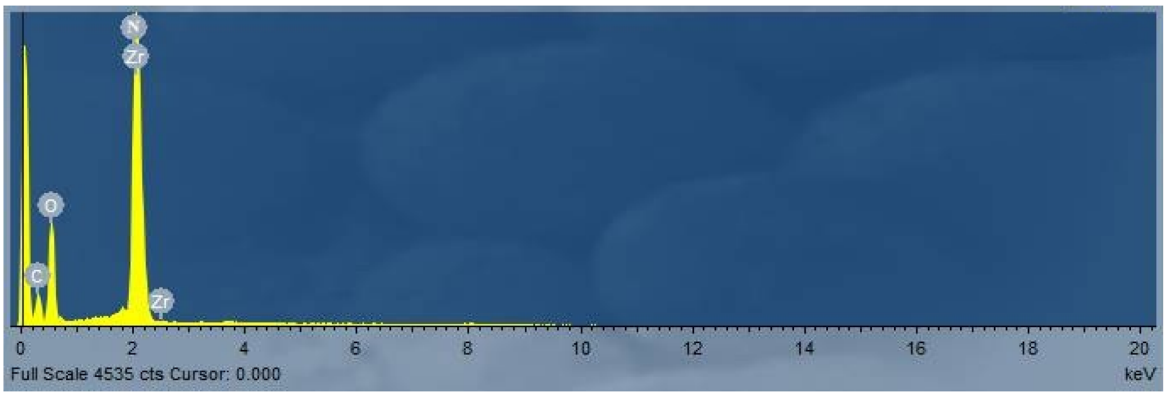

Fig. 3 EDX analysis of Zr-Vit B_3/MOF nanostructures.

Table 1 The crystallite size of Zr-Vit B_3/MOF using Debye–Scherer equation

2θ	FWHM	Crystallite size (nm)
14	0.152	55
16	0.145	57.8
17	0.245	34.26
18	0.264	31.8
21	0.164	51.5
24	0.154	55
26	0.214	39.8
30	0.231	37.3
39	0.210	41.9
46	0.190	47.4
52	0.190	48.6
59	0.220	43.1

the elemental composition, chemical structure, and purity of synthesized materials. In the case of the Zr-Vit B_3/MOF, EDX analysis confirmed the presence of zirconium (Zr), carbon (C), nitrogen (N), and oxygen (O). As shown in Fig. 3, no additional elemental peaks were detected, indicating the high purity of the synthesized MOF.

3.3. TEM analysis

Transmission electron microscopy (TEM) was employed to examine the surface morphology and particle size of the synthesized Zr-MOF. As shown in Fig. 4, the TEM image reveals a smooth, porous surface with particle sizes ranging from 27 to 52 nm.

3.4. XRD experimental data

The chemical structure of crystalline heterogeneous catalysts is often examined using XRD, which is nevertheless a highly useful technique for determining the crystalline components of solid catalysts in spite of this limitation. The average crystallite size of the Zr-MOF was estimated to be in the range of 34–57 nm based on calculations using the Debye–Scherrer equation[49,50] (Table 1), showing a great agreement with TEM analysis (Fig. 4). Fig. 5 reveals that the XRD spectrum of Zr-Vit B_3/MOF demonstrated relative peaks at $(2\theta) = 14$, 24, 26, 30, 39, 46, 52, and 58°, which characteristic of an orthorhombic structure and shows a little deviation shifting at $(2\theta) = 16$, 17° from the simulated data to 18 and 21°.

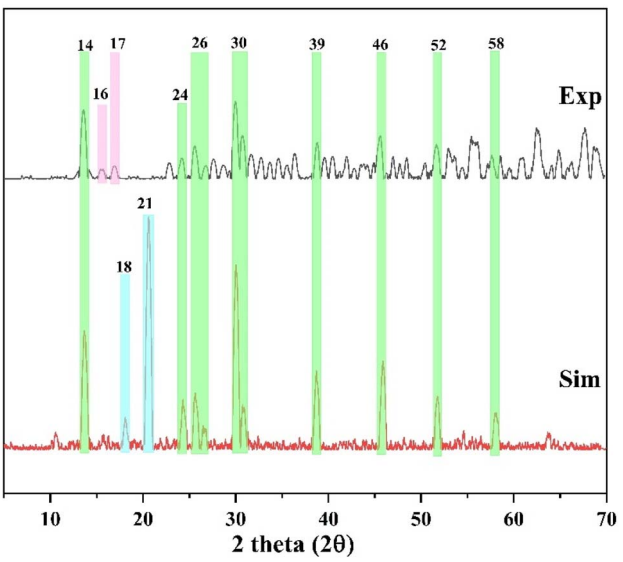

Fig. 5 Experimental and simulated XRD of Zr-Vit B_3/MOF nanostructures.

3.5. Computed crystal structures

As illustrated in Fig. 6a, which presents the predicted 3D ball-and-stick structure of Zr-Vit B_3/MOF, a zirconium atom is coordinated with four Vit B_3 molecules—three *via* their carboxylic acid (–COOH) groups and one through its nitrogen atom. The sequence was then again repeated to determine the Zr-Vit B_3/MOF crystal lattice. Using XRD data, a theoretical shape for the Zr-Vit B_3/MOF single crystal structure was inferred in Fig. 6b. The full crystal structure and full crystal lattice of Zr-Vit B_3/MOF, which crystallizes in an orthorhombic structure with high porosity and surface area, are shown in Fig. 6c and d.

3.6. Fourier transforms infrared (FTIR) spectra

Fig. 7 displays the synthesized Zr-Vit B3/MOF FTIR spectrum, where the carboxylic group is shown by bands at 1542 cm^{-1} and the Zr–O bond is indicated by bands at 1124 cm^{-1}.[51] The carboxyl groups from free aromatic carboxylic acid were detected at 1641 and 2082 cm^{-1}, and the carboxylate compounds that were coordinated with the zirconium metal center by $-CO_2$ asymmetrical stretching have peaks at 2854 and 2923 cm^{-1} and a bridging OH group that can be seen at 3452 cm^{-1}.[52]

3.7. Organic reaction

The porous zirconium-based MOF catalyst was investigated as a useful and efficient catalyst for the production of xanthene derivatives **3a–l**. One mole of aldehydes **1a–l** and two moles of dimedone (**2**) were put through a solvent-free one-pot condensation procedure at 60–70 °C. As a model reaction for reaction conditions optimization, benzaldehyde (**1a**) (1 mmol) and dimedone (**2**) (2 mmol) underwent a condensation process at 60–70 °C without the use of a solvent (Scheme 1).

When benzaldehyde (**1a**) (1 mmol) and dimedone (**2**) (2 mmol) were reacted under the same circumstances in the absence of catalyst, no discernible amount of product was produced (Table 2, entry 1). This suggests that for the reaction to begin, a catalyst needs to be present. However, the yield progressively rose when certain documented catalysts were employed to catalyze this kind of reaction (Table 2, entries 2–5).

According to the data acquired, using 50 mg of Zr/Vit B_3-MOF as a catalyst may result in the greatest yield when compound **3a** is produced. At 60–70 °C, the reaction takes 4 minutes to finish and yields 100% (Table 2, entry 6).

Based on the optimal reaction conditions, the range of this cyclization reaction was examined. Under solvent-free reaction conditions, dimedone (**2**) was reacted with a variety of

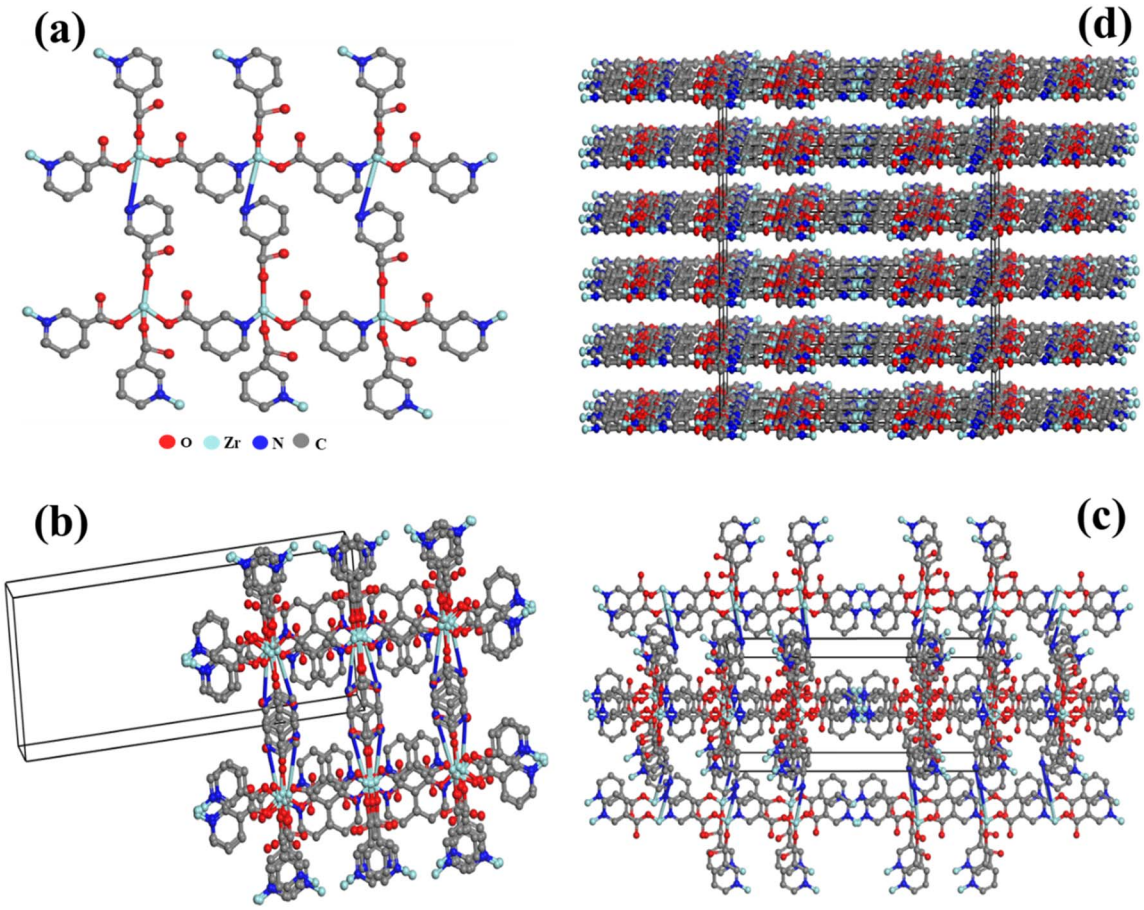

Fig. 6 (a) Zr-Vit B_3/MOF ball-stick crystal structure, (b) Zr-Vit B_3/MOF single crystal structure, (c) Zr-Vit B_3/MOF full crystal structure, and (d) Zr-Vit B_3/MOF crystal lattice.

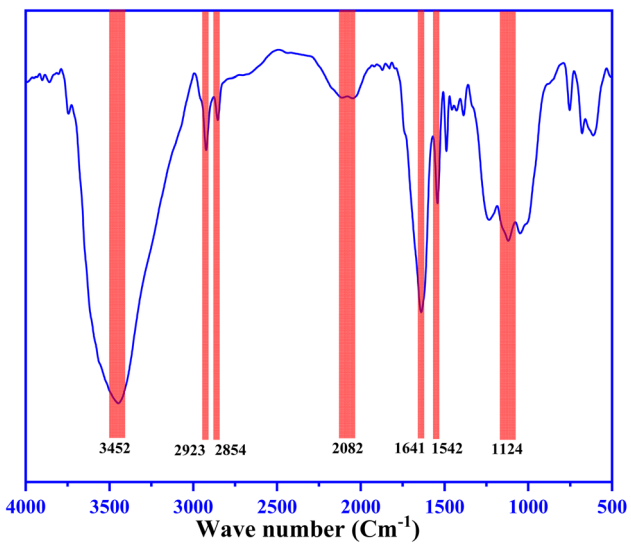

Fig. 7 IR-spectrum of Zr-Vit B_3/MOF nanostructures.

aldehydes **1a–l** that include groups that donate and withdraw electrons when Zr/Vit B_3-MOF was present (Table 3). Aromatic aldehydes having both electron-donating and electron-withdrawing substituents showed superior activity. All of the results are summarized in Table 3.

Table 2 The 1,8-dioxo-octahydroxanthene derivative (**3a**) was synthesized *via* reaction optimization with benzaldehyde (1 mmol) and dimedone (2 mmol)

Entry	Catalyst	Solvent	Time (min)	Yield (%)
1	—	—	180	No reaction
2	Silica	—	80	40
3	$Fe_2(SO_4)_3 \cdot 7H_2O$	—	90	86
4	V_2O_5/SiO_2	—	60	65
5	Fe_3O_4@SiO_2–SO_3H	—	4	97
6	ZrO_2 NPs	—	20	85
7	$Zr(HSO_4)_4$-MOF	—	40	86
8	Cu·BTC-MOF	—	15	92
9	**Zr/Vit B_3-MOF**	—	**4**	**98**

As shown in Table 4, the efficacy and environmental friendliness of the current process were assessed by comparing the outcomes of the synthesis of xanthene derivative **3a** with the most important information from the literature. It was discovered that several previously published techniques had one or more issues, including the use of hazardous and volatile organic solvents, high temperatures, long reaction times, and

Table 3 Zr-Vit B_3/MOF catalyzed synthesis of various derivatives of xanthenes **3a–l**

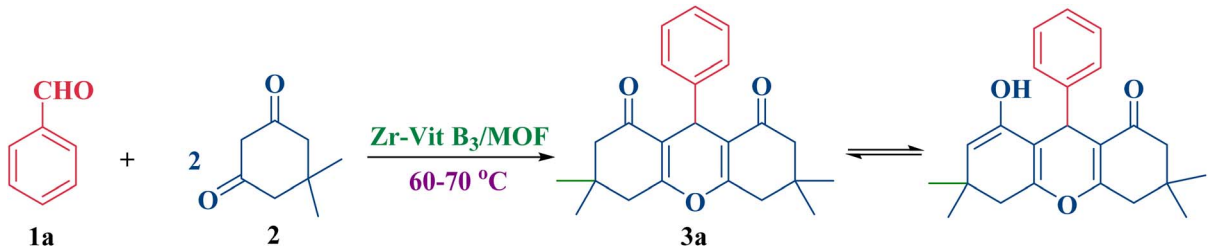

Entry	Aldehyde	Product	Product structure	Time (min)	Yield (%)	Measured M.P. (°C)	Reported M.P. (°C)/ref.
1	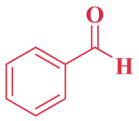	**3a**	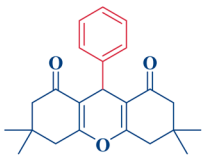	8	98	204–206	205–206/53
2	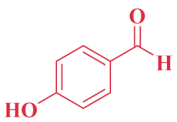	**3b**	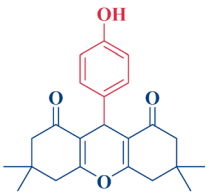	12	96	244–246	245–247/54
3	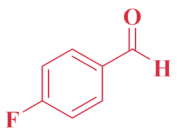	**3c**	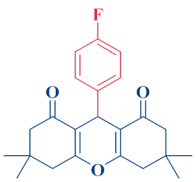	10	95	234–236	235–236/55
4	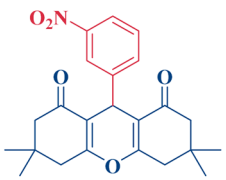	**3d**	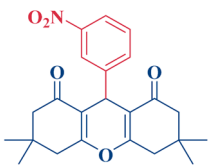	12	93	168–170	168–170/55
5	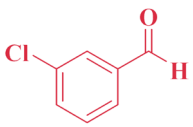	**3e**	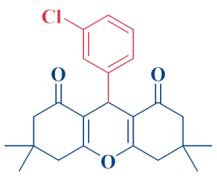	20	94	188–190	190–192/56
6	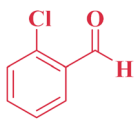	**3f**	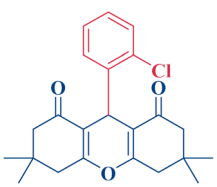	25	96	228–230	228–230/56
7	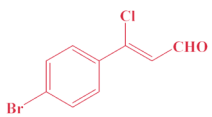	**3g**	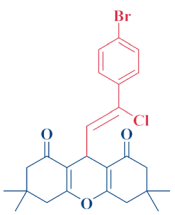	35	90	260–262	—

Table 3 (*Contd.*)

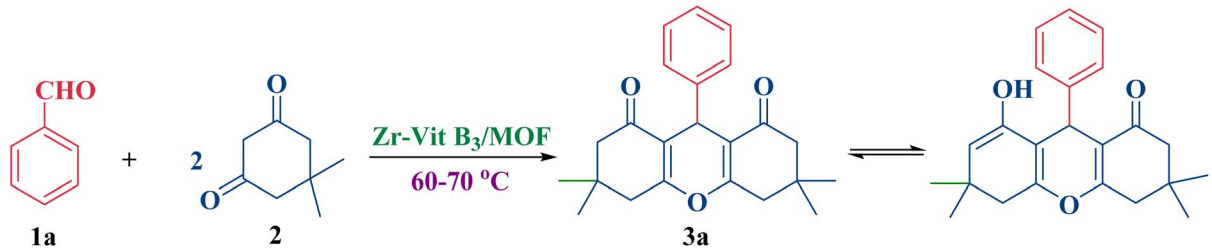

Entry	Aldehyde	Product	Product structure	Time (min)	Yield (%)	Measured M.P. (°C)	Reported M.P. (°C)/ref.
8	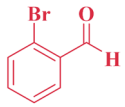	**3h**	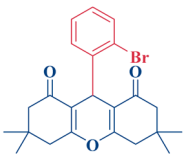	30	93	220–222	221–223/56
9	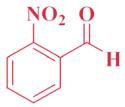	**3i**	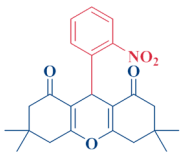	30	94	203–205	203–205/56
10	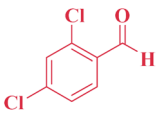	**3j**	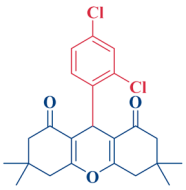	22	90	254–256	254–255/56
11	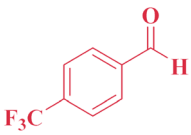	**3k**	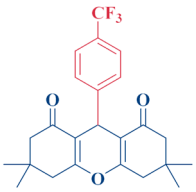	20	90	128–130	130–132/57
12	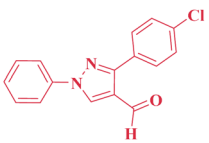	**3l**	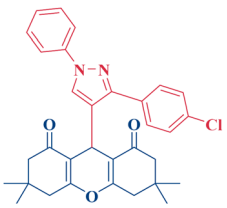	25	92	280–282	281–283/58

an excessive amount of catalyst. The current approach lessens the drawbacks of the previously published approaches. The influence of substituents on the reaction of aromatic aldehydes was evaluated, and empirical data confirmed that steric hindrance affected the reaction time, as observed in compounds **3g**, **3j**, and **3k**. This is particularly relevant for applications involving the tetragonal structure of the resulting MOF catalyst. Additionally, electron-withdrawing groups on the aldehyde ring, such as nitro group, enhanced the electrophilicity of the carbonyl carbon.

A believable process for the synthesis of several xanthene derivatives was shown in Scheme 2. Zr-Vit B_3/MOF significant oxophilicity suggests that it has a more potent catalytic role. First, the carbonyl group of the aromatic aldehyde coordinates with the Zr-Vit B_3/MOF to facilitate the nucleophilic attack.

The Knoevenagel product **A** is then produced when the aldehyde's carbonyl carbon atom is attacked by the nucleophilic dimedone (2). After adding **A** to **2** once more, the acyclic adduct intermediates are created, and intramolecular cyclization involving two hydroxyl groups results in the xanthene derivative **3g**.

Table 4 The Zr-Vit B_3/MOF catalyst was compared with other catalysts previously reported for the synthesis of 1,8-dioxo-octahydroxanthene derivative (**3a**)

Entry	Catalyst	Solvent	Time (h:min)	Yield (%)/ref.
1	Silica-BSSA	EtOH	10:00	98/59
2	$Fe_2(SO_4)_3 \cdot 7H_2O$	—	1:30	86/60
3	Nano-ZnO	—	2:00	Trace/61
4	Nano titania-supported sulfonic acid (n-TSA)	—	1:10	91/61
5	**Zr-Vit B_3/MOF**	**—**	**00:04**	**98/This work**

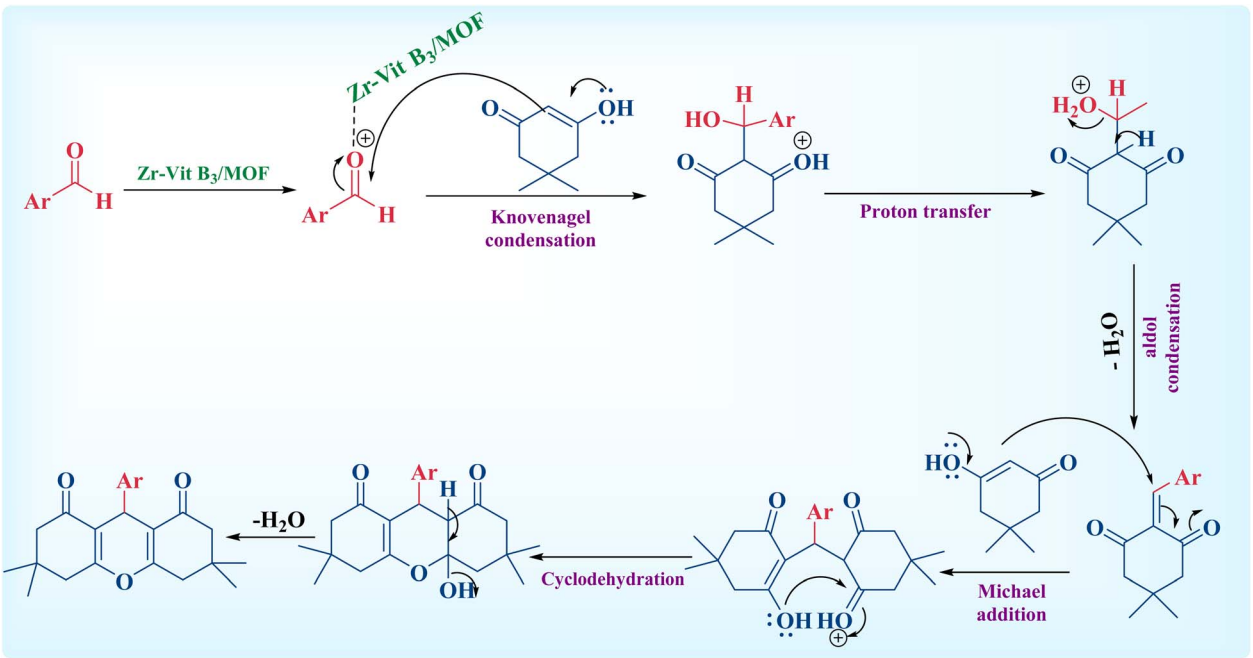

Scheme 2 A suggested mechanism for the synthesis of 1,8-dioxo-octahydroxanthene derivatives catalyzed by Zr-MOF.

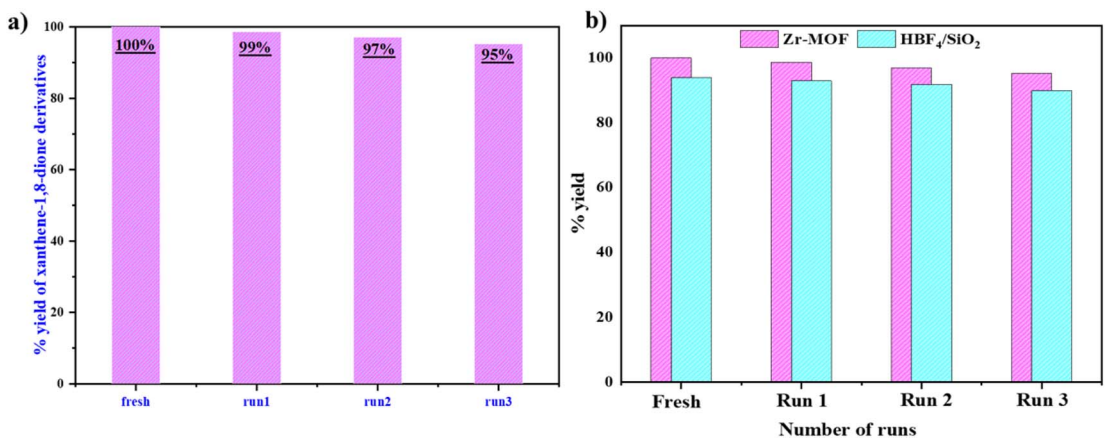

Fig. 8 (a) Reusability effect of Zr-Vit B_3/MOF catalyst and (b) comparing results with HBF_4–SiO_2 catalyst.

3.8. Reusability study

In our process, when the catalytic reaction was completed, Zr-MOF may be recovered conveniently from the reaction mixture and used further for the next cycle without activation, only through filtration and subsequent washing with ethyl acetate. Efforts were made to examine the reusability of Zr-MOF (Fig. 8a), which was found to be reusable at least three times. The figure shows that after three applications, the catalyst's catalytic activity drops from 100% to 95% as the number of catalysts used for the process increases,[62] due to deactivation

Table 5 Comparison of *E*-scores between xanthene derivatives and the reference molecule nevirapine

Ligand	HIV 1–RNA	Transcriptase
3a	−5.55	−6.52
3b	−5.69	−6.70
3c	−5.59	−6.61
3d	−6.09	−6.62
3e	−5.63	−6.62
3f	−5.64	−6.79
3g	−6.09	−5.90
3h	−5.78	−7.11
3i	−5.68	−6.68
3j	−5.73	−7.08
3k	−5.67	−6.47
3l	−6.40	−6.46
Zr-MOF	−12.32	−5.32
Nevirapine	−4.98	−6.96

a large number of catalyst's surface active sites. By comparing our results with another catalyst from literature, HBF_4–SiO_2 (ref. 63) (Fig. 8b), we see that our catalyst after three cycles dropped to 95%, while the other catalyst was near 87%.

3.9. Molecular docking validation

Our biological evaluations begin with the molecular docking program.[22,27,29,31,36–46] HIV is classified as a retrovirus that harms the human immune system and causes AIDS. According to recent statistics, approximately 38 million people are infected with the virus, and approximately 33 million people have lost their lives as a result of HIV-1.[64]

The active HIV-1 reverse transcriptase (RT) enzyme is formed through a structural maturation process that requires reorganization of subdomains and the creation of a p66/p66 homodimer. The HIV-1 retroviral transcriptase enzyme was the first to be successfully targeted by a drug, and its inhibition remains the basis of HIV treatment. Two types of inhibitors have demonstrated proven efficacy in clinical use: nucleoside reverse transcriptase inhibitors (NRTIs) and non-nucleoside reverse transcriptase inhibitors (NNRTIs). NRTIs are typically phosphorylated intracellularly, where they bind to the enzyme's active site so they can fuse with the leading end, whereas NNRTIs interact with an available dynamic site, not found in uncomplexed enzyme structures. Inhibitors targeting the specific active site of the RT RNase H domain have also been developed, but have not yet demonstrated sufficient efficacy to advance to clinical use. As examples of guidance in the work presented, dolutegravir inhibits integrase, while nevirapine acts as a transcription inhibitor. Although all the known antiviral agents have contributed to reducing mortality from this virus, the virus has a significant capacity to mutate. This suggests that no drug is currently completely effective. Therefore, in this work, we present a promising proposal for transcription and RNA inhibitors.[65]

The compounds being analyzed (prepared xanthenes/nevirapine) bind to the RNA strand groove, which spans nine base pairs. This is achieved by forming hydrogen bonds with the phosphate groups on either side of the groove, causing changes in the RNA's GGA conformation. The data in Table 5 presents the *E*-score calculation, which indicates the strength of binding between the main groove of HIV-1 and RNA Zr-Vit B_3 MOF, the prepared xanthene derivatives, in comparison to the reference molecule nevirapine.

The results underscore the exceptional potential of the synthesized Zr-MOF, which demonstrated unexpectedly strong binding to HIV-1 RNA, as reflected by a remarkably low binding energy score of −12.32 kcal mol^{-1}—suggesting enhanced stability and binding affinity with promising therapeutic potential compared to the reference drug nevirapine, which exhibited a higher *E*-score of −4.98 kcal mol^{-1}. This strong binding is likely due to robust interactions such as hydrogen bonding with phosphate groups flanking the RNA's major

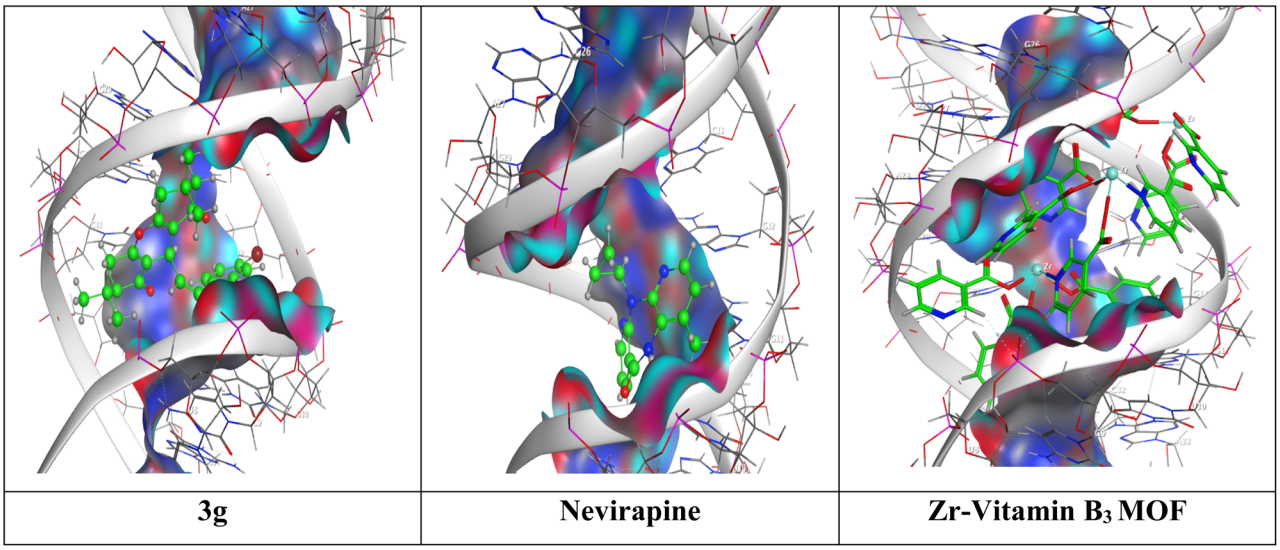

Fig. 9 The interaction between **3g** and nevirapine HIV-1 RNA.

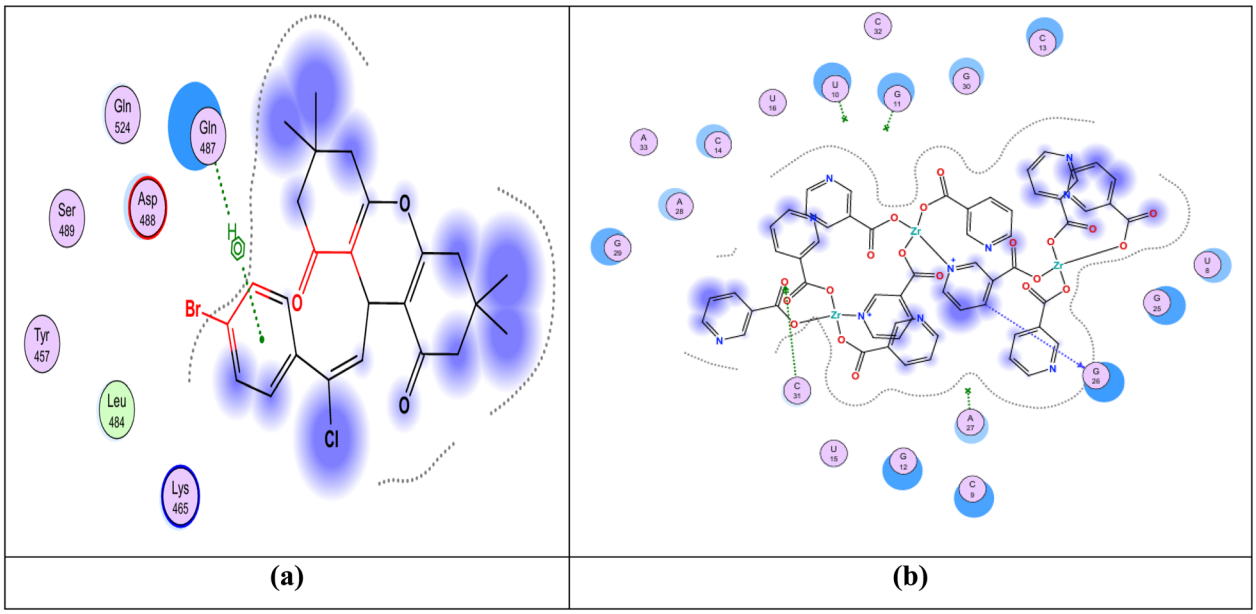

Fig. 10 (a) The active site in transcriptase liked with **3g**, (b) Zr-MOF binding with HIV-RNA groove.

groove, potentially triggering conformational changes in structurally significant regions like the GAGA bulge. While Zr-MOF's interaction with reverse transcriptase (RT) was comparatively weak (-5.32 kcal mol^{-1}), several of the xanthene-based ligands exhibited promising dual activity. In particular, compounds **3h**, **3j**, and **3f** displayed stronger RT binding than nevirapine, with **3h** and **3j** showing notably strong affinities for both RNA and RT, making them promising candidates for multi-target inhibition (Table 5). Additionally, ligands like **3l**, **3d**, and **3g** demonstrated superior RNA binding, suggesting a potential for specific RNA interference. The findings suggest a dual strategic potential: Zr-MOF as a specialized RNA binder that may act early in the viral life cycle, and xanthene derivatives as multi-target agents that could inhibit both viral RNA structure and enzymatic function. This dual-targeting approach could enhance antiviral efficacy and reduce the likelihood of resistance, positioning these novel compounds as promising leads in future HIV therapeutic development (Fig. 9).

Reverse transcriptase converts viral RNA into DNA in a process known as reverse transcription. Examples of viruses that contain reverse transcriptase include HIV and hepatitis B. Using this type of enzyme, viruses can replicate their genomes, allowing information to be transferred from RNA to DNA. Fig. 10b explains the good binding interaction between Zr-MOF and the HIV-RNA groove. The data in Fig. 10a show the protein residues present in the active site of reverse transcriptase, indicating that the **3g** has many sites that can form binding with the targeted enzyme. The strength of the binding can be measured, as shown in Table 5.

Pharmacophore calculation plays a crucial role in molecular docking by identifying key interaction features that a ligand must possess to bind effectively to a target. Features like ACC (hydrogen bond acceptor) ensure the ligand can form essential hydrogen bonds with donor residues in the protein as in Fig. 11 there are 8 ACC position, while PIN (positive ionizable)

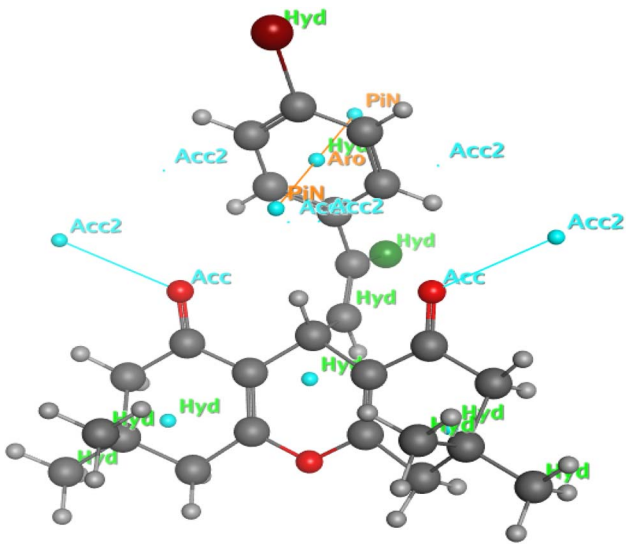

Fig. 11 Pharmacophore calculation.

highlights groups that interact with negatively charged sites. ARO (aromatic ring) helps align ligands with π–π stacking or other aromatic interactions crucial for stability, and HYD (hydrophobic region) ensures compatibility with non-polar pockets in the binding site as in Fig. 11 there are 11 HYD position. Including these pharmacophore elements in docking enhances pose prediction, improves screening accuracy, and ensures biologically meaningful interactions are preserved.

4. Conclusion

The study successfully demonstrated the green, cost-effective microwave-assisted synthesis of Zr-based metal–organic

framework (Zr-MOF) nanoparticles, which were thoroughly characterized using IR, SEM, TEM, EDX, and XRD techniques. The synthesized Zr-MOF exhibited excellent catalytic activity in the one-pot synthesis of tetrahydro xanthene-1,8-dione scaffolds and showed remarkable potential as an anti-HIV agent. Molecular docking results revealed an exceptionally high binding affinity of Zr-MOF to the HIV-1 frameshift site RNA (*E*-score: -12.32 kcal mol^{-1}), significantly surpassing the reference drug nevirapine (-4.98 kcal mol^{-1}). This strong RNA interaction suggests a potential mechanism of action through structural disruption of viral RNA. Although Zr-MOF showed comparatively weaker binding to reverse transcriptase, its interaction with both integrase and transcriptase enzymes still indicates a broad-spectrum inhibitory potential. Furthermore, xanthene-derived ligands, particularly compounds **3h** and **3j**, displayed strong dual-target binding to both RNA and RT, outperforming nevirapine and suggesting their suitability for multi-target antiviral strategies. Collectively, these findings position Zr-MOF as a promising RNA-specific inhibitor and highlight selected xanthene derivatives as strong candidates for further development in HIV-1 therapeutic interventions.

Data availability

The data supporting this article have been included as part of the ESI.†

Conflicts of interest

There are no conflicts to declare.

Acknowledgements

This research was funded by the Deanship of Scientific Research at King Saud University through Vice Deanship of Scientific Research Chairs; (Drug Exploration and Development Chair), project no. (MED-P-S-02-2025-12).

References

1 K. Chibale, M. Visser, D. van Schalkwyk, P. J. Smith, A. Saravanamuthu and A. H. Fairlamb, *Tetrahedron*, 2003, **59**, 2289–2296.
2 M. Maia, F. Durães, D. I. Resende, N. Szemerédi, L. Gales, P. Martins-da-Costa, M. Pinto, G. Spengler and E. Sousa, *Drugs and Drug Candidates*, 2022, **1**, 29–42.
3 K. Reddi Mohan Naidu, B. Satheesh Krishna, M. Anil Kumar, P. Arulselvan, S. Ibrahim Khalivulla and O. Lasekan, *Molecules*, 2012, **17**, 7543–7555.
4 S. A. Hilderbrand and R. Weissleder, *Tetrahedron Lett.*, 2007, **48**, 4383–4385.
5 X. Zhao, Y. Wang, X. Gao, X. Gao, M. Wang, H. Huang and B. Liu, *Chin. Chem. Lett.*, 2025, **36**, 109901.
6 S. T. Buck, F. Bettanin, E. Orestes, P. Homem-de-Mello, H. Imasato, R. B. Viana, J. R. Perussi and A. B. da Silva, *J. Chem.*, 2017, **2017**, 7365263.
7 T. Ebaston, F. Nakonechny, E. Talalai, G. Gellerman and L. Patsenker, *Dyes Pigm.*, 2021, **184**, 108854.
8 S. Samanta, K. Lai, F. Wu, Y. Liu, S. Cai, X. Yang, J. Qu and Z. Yang, *Chem. Soc. Rev.*, 2023, **52**, 7197–7261.
9 G. Pohlers, J. Scaiano and R. Sinta, *Chem. Mater.*, 1997, **9**, 3222–3230.
10 C. G. Knight and T. Stephens, *Biochem. J.*, 1989, **258**, 683–687.
11 E. Klimtchuk, M. Rodgers and D. Neckers, *J. Phys. Chem.*, 1992, **96**, 9817–9820.
12 G. Saint-Ruf and J.-P. Poupelin, *Naturwissenschaften*, 1975, **62**, 584–585.
13 F. Mohamadpour, *Indian J. Chem.*, 2019, **58B**, 832–841.
14 R. Hosseinzadeh-Khanmiri, E. Vessally, G. H. Shahverdizadeh, L. Edjlali and M. Babazadeh, *Iran. J. Chem. Chem. Eng.*, 2018, **37**(3), 51–62.
15 F. Rajabi, M. Abdollahi, E. S. Diarjani, M. G. Osmolowsky, O. M. Osmolovskaya, P. Gómez-López, A. R. Puente-Santiago and R. Luque, *Materials*, 2019, **12**, 2386.
16 R. J. Sarma and J. B. Baruah, *Dyes Pigm.*, 2005, **64**, 91–92.
17 M. Seyyedhamzeh, P. Mirzaei and A. Bazgir, *Dyes Pigm.*, 2008, **76**, 836–839.
18 F. Shirini and N. G. Khaligh, *Dyes Pigm.*, 2012, **95**, 789–794.
19 B. Rajitha, B. S. Kumar, Y. T. Reddy, P. N. Reddy and N. Sreenivasulu, *Tetrahedron Lett.*, 2005, **46**, 8691–8693.
20 A. G. Banerjee, L. P. Kothapalli, P. A. Sharma, A. B. Thomas, R. K. Nanda, S. K. Shrivastava and V. V. Khatanglekar, *Arabian J. Chem.*, 2016, **9**, S480–S489.
21 S. A. E. Naser, K. O. Badmus and L. Khotseng, *Coatings*, 2023, **13**, 1456.
22 G. E. Said, M. Tarek, A. A. Zen, A. A. Almehizia, A. M. Naglah and T. K. Khatab, *J. Organomet. Chem.*, 2024, **1008**, 123074.
23 S.-L. Kang, T. Yue, D.-D. Su, W.-J. Shi, P.-C. Jiang and Z.-H. Zhang, *ACS Sustain. Chem. Eng.*, 2024, **12**, 18200–18210.
24 W.-J. Li, Z.-Q. Wang, J.-B. Wang, R. Wu, H.-W. Shi, E.-X. Liu, M. Zhang and Z.-H. Zhang, *J. Catal.*, 2024, **430**, 115308.
25 W.-J. Li, J.-B. Wang, Y.-H. Liu, M. Zhang and Z.-H. Zhang, *Chin. Chem. Lett.*, 2025, **36**, 110001.
26 A. R. Silva, J. Y. Alexandre, J. E. Souza, J. G. L. Neto, P. G. de Sousa Júnior, M. V. Rocha and J. C. Dos Santos, *Molecules*, 2022, **27**, 4529.
27 G. E. Said, M. Tarek, A. S. Al-Wasidi, A. M. Naglah, A. A. Almehizia and T. K. Khatab, *J. Mol. Struct.*, 2024, **1311**, 138462.
28 V. Pascanu, G. González Miera, A. K. Inge and B. Martín-Matute, *J. Am. Chem. Soc.*, 2019, **141**, 7223–7234.
29 A. S. Al-Wasidi, H. M. AlMohisen, A. A. Almehizia, A. M. Naglah, M. Tarek, G. E. Said and T. K. Khatab, *J. Mol. Struct.*, 2024, **1317**, 139120.
30 S. Dutt, A. Kumar and S. Singh, *Clean Technol.*, 2023, **5**, 140–166.
31 A. S. Al-Wasidi, M. Tarek, G. E. Said, A. M. Naglah, A. A. Almehizia and T. K. Khatab, *RSC Adv.*, 2024, **14**, 20454–20465.
32 D. E. Ward, *The AmFAR AIDS handbook: the complete guide to understanding HIV and AIDS*, WW Norton & Company, 1999.
33 E. Lefebvre and C. A. Schiffer, *AIDS Rev.*, 2008, **10**, 131.

34 D. S. Schiller and M. Youssef-Bessler, *Clin. Ther.*, 2009, **31**, 692–704.
35 S. Palmer, F. Maldarelli, A. Wiegand, B. Bernstein, G. J. Hanna, S. C. Brun, D. J. Kempf, J. W. Mellors, J. M. Coffin and M. S. King, *Proc. Natl. Acad. Sci. U. S. A.*, 2008, **105**, 3879–3884.
36 T. K. Khatab, K. A. El-Bayouki and W. M. Basyouni, *Tetrahedron Lett.*, 2011, **52**, 1448–1451.
37 T. K. Khatab, A. Abdelghany and H. A. Soliman, *Silicon*, 2018, **10**, 703–708.
38 H. A. Soliman, T. K. Khatab and F. M. Abdel-Megeid, *Chin. Chem. Lett.*, 2016, **27**, 1515–1518.
39 T. K. Khatab, K. A. M. El-Bayouki, W. M. Basyouni and F. M. Sroor, *Egypt. J. Chem.*, 2013, **56**, 291–305.
40 T. K. Khatab, S. S. Elmorsy and D. S. Badawy, *Phosphorus, Sulfur Silicon Relat. Elem.*, 2005, **180**, 109–116.
41 T. K. Khatab, K. A. EI-Bayouki, W. M. Basyouni, F. A. El-Basyoni, M. M. Ali, S. Y. Abbas and E. A. Mostafa, *Res. J. Pharm., Biol. Chem. Sci.*, 2015, **6**, 281–291.
42 S. S. Elmorsy, D. S. Badawy and T. K. Khatab, *Phosphorus, Sulfur Silicon Relat. Elem.*, 2006, **181**, 2005–2012.
43 N. Shaker, E. M. Kandil, Y. Osama, T. K. Khatab and M. E. Khalifa, *Curr. Org. Chem.*, 2021, **25**, 2037–2044.
44 G. E. Said, H. M. Metwally, E. Abdel-Latif, M. R. Elnagar, H. S. Ibrahim and M. A. Ibrahim, *Bioorg. Chem.*, 2024, **151**, 107666.
45 M. Tarek, T. K. Khatab, A. A. Almehizia, A. M. Naglah, A. A. Zen and G. E. Said, *Polyhedron*, 2025, **268**, 117361.
46 G. E. Said, M. Tarek, A. A. Almehizia, A. M. Naglah, H. A. Ghabbour and T. K. Khatab, *J. Organomet. Chem.*, 2025, 123623.
47 J. Klinowski, F. A. A. Paz, P. Silva and J. Rocha, *Dalton Trans.*, 2011, **40**, 321–330.
48 I. Thomas-Hillman, A. Laybourn, C. Dodds and S. W. Kingman, *J. Mater. Chem. A*, 2018, **6**, 11564–11581.
49 L. Magson, H. Hölzel, A. S. Aslam, S. Henninger, G. Munz, K. Moth-Poulsen, M. Knaebbeler-Buss, I. Funes-Ardoiz and D. Sampedro, *ACS Appl. Mater. Interfaces*, 2024, **16**, 7211–7218.
50 C. Cretu, R. Nicola, S.-A. Marinescu, E.-M. Picioruș, M. Suba, C. Duda-Seiman, A. Len, L. Illés, Z. E. Horváth and A.-M. Putz, *Int. J. Mol. Sci.*, 2023, **24**, 13887.
51 N. Fiuza-Maneiro, K. Sun, I. Lopez-Fernandez, S. Gomez-Grana, P. Muller-Buschbaum and L. Polavarapu, *ACS Energy Lett.*, 2023, **8**, 1152–1191.
52 K. I. Hadjiivanov, D. A. Panayotov, M. Y. Mihaylov, E. Z. Ivanova, K. K. Chakarova, S. M. Andonova and N. L. Drenchev, *Chem. Rev.*, 2020, **121**, 1286–1424.
53 F. Shirini, M. Abedini and R. Pourhasan, *Dyes Pigm.*, 2013, **99**, 250–255.
54 A. Zare, A. R. Moosavi-Zare, M. Merajoddin, M. A. Zolfigol, T. Hekmat-Zadeh, A. Hasaninejad, A. Khazaei, M. Mokhlesi, V. Khakyzadeh and F. Derakhshan-Panah, *J. Mol. Liq.*, 2012, **167**, 69–77.
55 A. Khazaei, A. R. Moosavi-Zare, Z. Mohammadi, A. Zare, V. Khakyzadeh and G. Darvishi, *RSC Adv.*, 2013, **3**, 1323–1326.
56 I. Mohammadpoor-Baltork, M. Moghadam, V. Mirkhani, S. Tangestaninejad and H. R. Tavakoli, *Chin. Chem. Lett.*, 2011, **22**, 9–12.
57 F. Darviche, S. Balalaie, F. Chadegani and P. Salehi, *Synth. Commun.*, 2007, **37**, 1059–1066.
58 M. Nikpassand and L. Zare Fekri, *Russ. J. Gen. Chem.*, 2017, **87**, 816–820.
59 K. Niknam, F. Panahi, D. Saberi and M. Mohagheghnejad, *J. Heterocycl. Chem.*, 2010, **47**, 292–300.
60 R. Khoeiniha, A. Ezabadi and A. Olyaei, *Iran. Chem. Commun.*, 2016, **4**, 273–282.
61 A. Amoozadeh, S. F. Hosseininya and S. Rahmani, *Res. Chem. Intermed.*, 2018, **44**, 991–1011.
62 M. Bagherzadeh, M. Chegeni, A. Bayrami and M. Amini, *Sci. Rep.*, 2024, **14**, 17730.
63 B. P. Bandgar, S. S. Gawande, S. C. Warangkar and J. V. Totre, *Bioorg. Med. Chem.*, 2010, **18**, 3618–3624.
64 O. Abdollahi, A. Mahboubi, Z. Hajimahdi and A. Zarghi, *Iran. J. Pharm. Res.*, 2022, **21**, e126562.
65 T. W. Kirby, S. A. Gabel, E. F. DeRose, L. Perera, J. M. Krahn, L. C. Pedersen and R. E. London, *Biomolecules*, 2023, **13**, 1603.